Along-Track Deformation Retrieval Performance With the ROSE-L Multichannel SAR System Using Two-Look ScanSAR

Simon Trumpf, Pau Prats-Iraola, *Fellow, IEEE*, and Alberto Moreira, *Fellow, IEEE*

***Abstract*— A new generation of spaceborne synthetic aperture radar (SAR) systems with digital beamforming capabilities is currently under development. In particular, multiple azimuth channels provide access to a large Doppler bandwidth, which can be used to improve the azimuth resolution. In the ScanSAR mode, however, the resolution is given by the burst time. However, the exploitation of a large Doppler bandwidth leads to a wider azimuth coverage and, therefore, to a larger overlap between consecutive bursts. This overlap can be exploited interferometrically in order to retrieve an improved measurement of the azimuth differential shift between two acquisitions. The retrieval performance is hereby limited by the antenna pattern, which can severely deteriorate the image quality toward the edges of the extended bursts. The reduced quality leads to a decreased deformation retrieval accuracy in these parts of the acquisition. We analyze the performance of the along-track deformation retrieval using a two-look ScanSAR processing for the particular case of the upcoming ROSE-L mission. For this purpose, we analyze the influences of thermal noise and azimuth ambiguities on the performance and show their impact on the retrieval. The derived performance is validated with simulations using distributed targets and realistic scenes. The results show that the retrieval is subject to a tradeoff between spatial resolution and retrieval accuracy. However, even for low multilooking factors, the azimuth displacement is retrieved with better accuracy than single-look approaches. The retrieval accuracy is also shown to be sufficient in most cases in order to decouple the along-track and across-track components of the deformation at medium resolutions. In this way, the phase jumps between bursts usually observed in interferograms of nonstationary scenes are significantly mitigated.**

***Index Terms*— ScanSAR, synthetic aperture radar (SAR) interferometry, two-look ScanSAR.**

I. Introduction

EARTH surface deformation measurements are one of the numerous applications of synthetic aperture radar (SAR) and are frequently used for observing tectonic and volcanic processes [1], [2], [3]. Existing SAR systems are often limited by their quasi-polar orbits, which limit the accuracy with which deformations in the north–south direction can be measured using interferometry. As a technique to overcome this limitation in burst acquisition modes, a two-look mode, which is an extension of the spectral diversity [4] or multiaperture InSAR (MAI) [5] techniques applied to the ScanSAR mode, is often used. ScanSAR is a wide-swath acquisition mode, which increases the coverage at the expense of resolution by sharing the synthetic aperture time among several subswaths [6]. The two-look technique exploits overlapping areas of neighboring bursts to obtain images from different azimuth look angles or squints and thus exploit this angular diversity in order to retrieve the shifts along the azimuth direction. It has been validated with the TerraSAR-X and TanDEM-X satellites [7], [8], [9], however at the cost of a deteriorated azimuth resolution compared to the single-look mode. The same technique has been applied to Sentinel-1 acquisitions [10], [11], [12], [13], whereby here only a limited coverage is achieved due to the small overlap areas of the bursts. Similar experiments have been conducted in the L band using ALOS-2 acquisitions [14].

The upcoming Radar Observing System for Europe at L-band (ROSE-L) mission [15], [16] features a SAR instrument that is suitable for exploiting a two-look processing approach on a larger scale without deteriorating the azimuth resolution. ROSE-L is part of the Copernicus Sentinel Expansion Program led by the European Commission and supported by the European Space Agency (ESA). The system uses ScanSAR in combination with multiple azimuth phase centers (MAPS) [17] as well as digital beamforming on receive in elevation, also known as scan-on-receive (SCORE) [18]. The accuracy of the two-look technique on the ROSE-L mission is limited by the deterioration of the signal quality toward the edges of the two-look bursts. This deterioration is caused by the low relative gain of the transmit antenna pattern in these areas, which results in a decreased signal-to-noise ratio (SNR) and azimuth-ambiguity-to-signal ratio (AASR) compared to the burst center.

Two-look processing for ROSE-L has also been proposed in [19], where different tapering configurations of the transmit antenna have been investigated in order to improve the image quality beyond the single-look Doppler bandwidth, obviously at the expense of a slight quality degradation for the single-look band. In contrast, this article focuses on a thorough analysis of a two-look processing strategy for deformation retrieval for the current configuration of the ROSE-L system, without changing the transmit antenna pattern and thus keeping the image quality levels for the single-look Doppler bandwidth. The work is hereby based on analytical evaluations as well as on end-to-end simulations. Even though this work

Received 22 April 2024; revised 5 October 2024 and 22 March 2025; accepted 26 March 2025. Date of publication 7 April 2025; date of current version 17 April 2025. *(Corresponding author: Simon Trumpf.)*

The authors are with the Microwave and Radar Institute, German Aerospace Center (DLR), 82234 Weßling, Germany (e-mail: Simon.Trumpf@dlr.de).

Digital Object Identifier 10.1109/TGRS.2025.3557542

focuses on the ROSE-L case, the principle of the analysis can also be applied for different system configurations.

This article is structured as follows. Section II introduces the principle of the two-look processing in the frame of the ROSE-L mission. Section III presents an analytical performance estimation for the azimuth deformation using the two-look approach, while Section IV presents the results of the end-to-end simulations. Finally, conclusions are drawn and an outlook is provided in Section V.

II. Two-Look Processing With ROSE-L

ScanSAR is the main acquisition mode for the ROSE-L system. ScanSAR is a wide-swath acquisition mode, where the antenna footprint on ground switches between several subswaths [6]. Within a subswath, the adjacent bursts are generally timed to have continuous ground coverage with a slight overlap between bursts. The ground coverage of a single burst hereby depends on the processed Doppler bandwidth, as further explained in Appendix A. In combination with ScanSAR, ROSE-L uses an antenna that is divided into five azimuth channels. Hereby, the pulse repetition frequency (PRF) is reduced in order to cover a wider swath, which also leads to each channel signal being undersampled. Hence, the first step during the on-ground processing is to perform the azimuth reconstruction of all N_{ch} channels with bandwidth PRF_{ch} in order to obtain one unaliased SAR image [17]. Digital processing algorithms as described in [20] are used such that, after the reconstruction step, a signal with bandwidth

$$B_{\text{rec}} = N_{\text{ch}} \cdot \text{PRF}_{\text{ch}} \tag{1}$$

is retrieved.

In order to obtain two looks for every point on ground, a doubling of the spatial coverage in azimuth for each burst is needed when compared to the single-look case. This requires the processing of a larger azimuth Doppler bandwidth, as derived in Appendix A, as well as a proper coverage of the two-look bandwidth by the antenna pattern. ROSE-L fulfills the basic requirements to apply a two-look processing technique as a large Doppler bandwidth is available for processing without changing the system parameters, as shown in Fig. 1 for the exemplary parameters given in Table I. In this table, R_0 is the slant-range distance, θ_{inc} is the mean incident angle, and v_{eff} is the effective platform velocity.

Note, however, that the ROSE-L system has been designed in order to meet certain requirements in terms of spatial coverage, spatial resolution, noise equivalent sigma zero (NESZ), and distributed target-to-ambiguity ratio (DTAR) considering only a one-look ScanSAR operation. These requirements are summarized in Table II. Only the central part of the Doppler spectrum within the 1.3-kHz interval meets these requirements, which is equivalent to a focused burst length of about 25 km with a very small overlap between consecutive bursts. When extending the processed bandwidth to obtain two looks, the interferometric performance will be especially limited by the two pattern minima located at around ± 1.8 kHz. The low gain will cause decorrelation due to a decreased SNR and increased AASR in the case of incoherent ambiguities, while

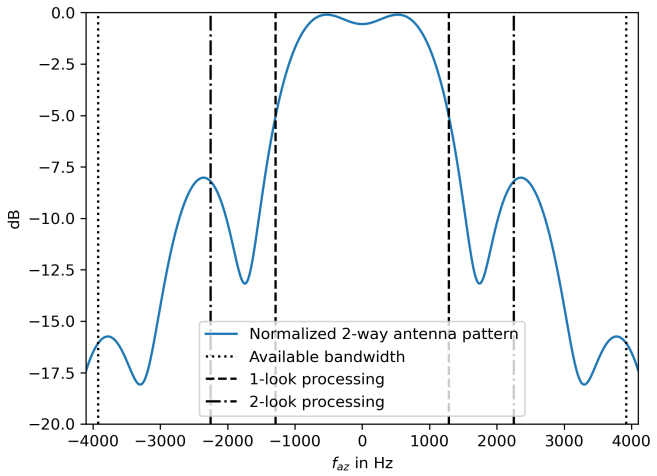

Fig. 1. Normalized two-way antenna pattern of the ROSE-L satellite in azimuth dimension. Assuming the parameter set of Table I, the vertical dotted lines enclose the available bandwidth after the MAPS reconstruction, the vertical dashed lines enclose the bandwidth used for the nominal single-look processing approach, and the vertical dashed-dotted lines enclose the bandwidth of the two-look ScanSAR approach used in this article.

TABLE I
Simulation Parameters for ROSE-L

Number of channels	N_{ch}	5
Effective platform velocity	v_{eff}	$7142.76\,\text{m}\,\text{s}^{-1}$
Sub-swath index		1 (nearest range)
Channel pulse repetition frequency	PRF_{ch}	1567.85 Hz
Slant-range distance of closest approach	R_0	804 km
Incident angle	θ_{inc}	32°
Azimuth Doppler bandwidth of a target	B_{target}	635 Hz

TABLE II
Requirements for the ROSE-L Interferometric Wide-Swath Mode [15]

Swath width	260 km
Resolution	$50\,\text{m}^2$
NESZ	<-28 dB
DTAR	<-23 dB

coherent ambiguities might introduce biases to the signal. The severity of these effects is further analyzed in the following.

By properly enlarging the processed Doppler bandwidth, each target on ground is covered with two adjacent bursts, hence automatically generating the two looks. In other words, a 50% overlap between consecutive bursts is achieved. By computing the difference of the interferometric phases of the two looks and performing the phase unwrapping, the unwrapped spectral diversity phase $\phi_{\text{sd,uw}}$ is obtained. The measured geometric shift in azimuth d_{at} is then proportional to the unwrapped spectral diversity phase of the two looks and given by [7], [8], [9], [14]

$$d_{\text{at}} = \phi_{\text{sd,uw}} \cdot \frac{v_g}{2\pi\,\Delta f} \tag{2}$$

where v_g is the platform velocity over ground and Δf is the spectral separation of the looks.

The retrieved azimuth shift can be used in addition to update the single-look interferogram in order to obtain the deformation in the zero-Doppler direction. This step effectively removes the phase jumps between consecutive bursts

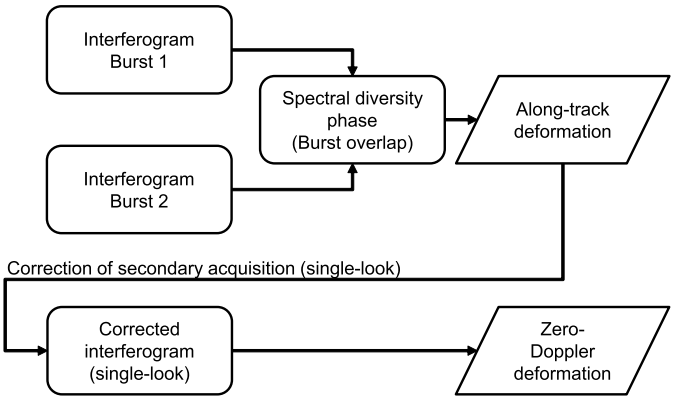

Fig. 2. Suggested processing chain to retrieve deformation estimates in the azimuth and zero-Doppler directions.

and eases the further processing of the single-look interferometric phase. As a result, the processing scheme provides two different deformation values for each radar pixel: a value for the azimuthal component of the deformation and a value for the zero-Doppler component of the deformation, i.e., the 2-D deformation in radar coordinates is retrieved. Note that, in general, the accuracy in the azimuthal direction is worse than the one in the zero-Doppler direction for two-look ScanSAR systems due to the different phase sensitivities to deformation. However, the two-look ScanSAR approach allows going beyond the accuracy one can achieve by solely exploiting the azimuth spatial resolution, as is implied in [21]. A scheme of the described processing strategy is shown in Fig. 2. Note that this figure presents a simplified scheme, where steps such as phase filtering and unwrapping have been omitted for the sake of simplicity.

By combining ascending and descending passes, it is then possible to compute the 3-D deformation (easting, northing, and vertical), e.g., by means of a conventional weighted least squares inversion [22]. One shall consider that the measurement in the azimuth direction will have in general a worse performance, as indicated in Section III. One possibility, as suggested next, is to achieve a similar accuracy as the line-of-sight measurement by using more looks when estimating the azimuth shift, i.e., at the expense of spatial resolution.

III. Performance Analysis

In order to analyze the performance of the deformation measurements we assume distributed Gaussian scatterers and derive the Cramér–Rao bound. For conventional SAR acquisitions, the optimal estimator for the azimuth shift is the cross correlation operation. Its Cramér–Rao bound is given by [21]

$$\sigma_{CC,CR} = \sqrt{\frac{3}{2N_{\text{looks}}}} \frac{\sqrt{1-\gamma^2}}{\pi\gamma} \frac{v_g}{B_{\text{target}}} \tag{3}$$

where N_{looks} is the effective number of averaged samples, γ is the interferometric coherence, and B_{target} is the target Doppler bandwidth. Note that the performance is limited by the azimuth resolution. The standard deviation of the two-look ScanSAR case can be derived equivalently to the one of the split-bandwidth case shown in [21]. While for the split-bandwidth case, a similar coherence can be assumed for both looks, this assumption does not hold here due to the significantly lower antenna gain around the minima of the normalized antenna pattern. The two looks are thus considered separately and the resulting standard deviation of the two-look measurement $\sigma_{2\text{LSC}}$ is computed as

$$\sigma_{2\text{LSC}} = \sqrt{\sigma_{L1}^2 + \sigma_{L2}^2}. \tag{4}$$

The standard deviation for each look follows the equation similar to the split-bandwidth case

$$\sigma_{L\{1,2\}} = \frac{1}{\sqrt{2N_{\text{looks}}}} \frac{\sqrt{1-\gamma_{L\{1,2\}}^2}}{\gamma_{L\{1,2\}}} \frac{v_g}{2\pi\,\Delta f} \tag{5}$$

where the subscript $L\{1, 2\}$ refers to the indices of the respective looks. The combination of both looks results in a two-look measurement accuracy of

$$\sigma_{2\text{LSC}} = \frac{1}{\sqrt{2N_{\text{looks}}}} \sqrt{\left(\frac{1-\gamma_{L1}^2}{\gamma_{L1}^2} + \frac{1-\gamma_{L2}^2}{\gamma_{L2}^2}\right)} \frac{v_g}{2\pi\,\Delta f}. \tag{6}$$

In order to properly determine the interferometric coherence of the looks, several factors have to be considered. Temporal changes, thermal noise, and azimuth ambiguities cause decorrelation, which deteriorates the signal quality, leading to worse estimates of the deformation. This is especially relevant here due to the decreasing gain of the antenna pattern in azimuth around the minima of the normalized antenna pattern, resulting in an increase of the noise and azimuth ambiguity levels. The decorrelation due to the SNR and the AASR are thus relevant measures for the performance analysis. Together with temporal decorrelation, γ_{TEMP}, the coherence model assumed for each look follows the equation of the well-known form:

$$\gamma_{L\{1,2\}} = \gamma_{\text{TEMP}} \cdot \gamma_{\text{SNR}\{1,2\}} \cdot \gamma_{\text{AASR}\{1,2\}}. \tag{7}$$

It is worth mentioning that this model assumes uncorrelated azimuth ambiguities. For small interferometric baselines, though, azimuth ambiguities will be in general coherent, and therefore, the performance model needs to be adapted accordingly. This particular aspect is addressed in Section III-E.

A. Decorrelation Due to Receiver Noise

Under the assumption of circular white Gaussian noise, the SNR depends on the power of the returned radar signal and the receiver noise power. Given the normalized radar backscatter coefficient in the ground range σ_0 and the Doppler-centroid-dependent NESZ, the SNR can be approximated as

$$\text{SNR}(f_{\text{DC}}) = \frac{\sigma_0}{\text{NESZ}(f_{\text{DC}})} \tag{8}$$

where f_{DC} represents the Doppler centroid. The NESZ hereby depends on the azimuth antenna pattern and is scaled with the MAPS reconstruction. Assuming a similar SNR for the primary and secondary acquisitions for a given look, the coherence is then computed as [23]

$$\gamma_{\text{SNR}}(f_{\text{DC}}) = \frac{1}{1+\text{SNR}^{-1}(f_{\text{DC}})}. \tag{9}$$

The derivation of the system's NESZ depending on the Doppler centroid f_{DC} is shown in Appendix B.

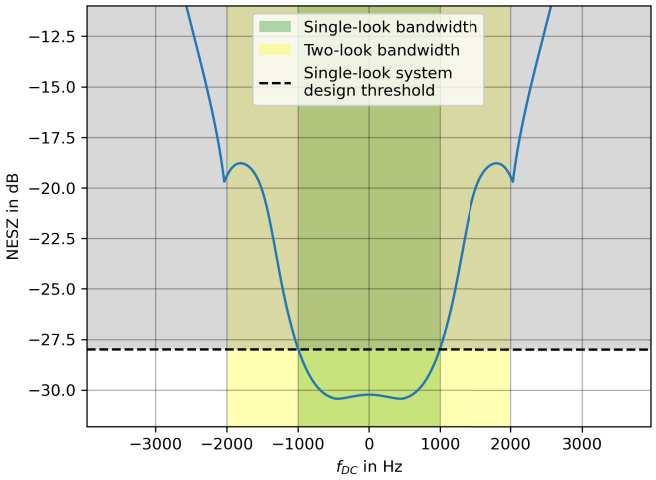

Fig. 3. NESZ after MAPS reconstruction over azimuth Doppler centroid frequency for the analytical performance computation. A PRF of 1567.85 Hz has been considered. The horizontal dashed line represents the single-look system design constraint for the NESZ, which is assumed to be fulfilled. Bandwidths of the single-look and two-look acquisition are marked in green and yellow, respectively.

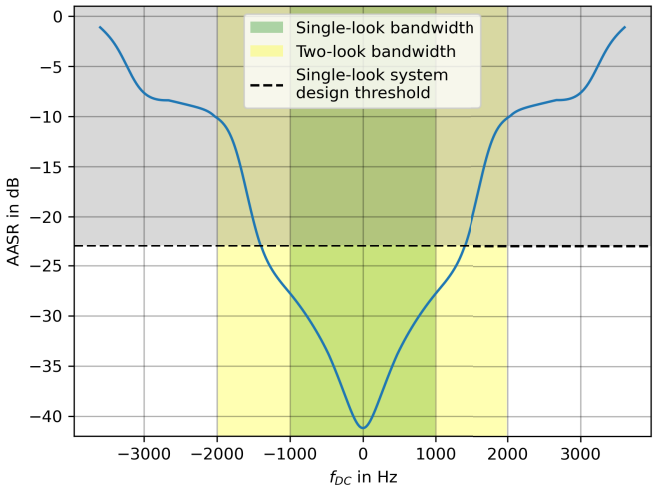

Fig. 4. AASR of ROSE-L computed from the antenna pattern after application of the azimuth reconstruction algorithm and focusing for a PRF of 1567.85 Hz. Single-look bandwidth and two-look bandwidth, as well as the system design threshold, are marked. Within the two-look bandwidth, the quality requirements of the single-look acquisition mode are violated.

B. Decorrelation Due to Incoherent Azimuth Ambiguities

Azimuth ambiguities may cause additional decorrelation as the signal power locally decreases, while the power of the ambiguities might not. Similar to the noise case, the AASR is assumed to be the same for the primary and secondary acquisitions of the same look. Just like the SNR, the AASR for ROSE-L varies as a function of the Doppler centroid of the target. It is computed by adding all the ambiguous contributions and dividing it by the main signal power such that [20]

$$\mathrm{AASR}(f_{\mathrm{DC}}) = \frac{p_a(f_{\mathrm{DC}})}{p_s(f_{\mathrm{DC}})} \tag{10}$$

where p_s and p_a are the total power contributions of the focused signal and its ambiguities. Hereby, the MAPS reconstruction has to be considered, which reconstructs the signal in $N_{\mathrm{ch}} = 5$ different intervals as further explained in Appendix C. The coherence due to the AASR is finally given by [24]

$$\gamma_{\mathrm{AASR}}(f_{\mathrm{DC}}) = \frac{1}{1 + \mathrm{AASR}(f_{\mathrm{DC}})}. \tag{11}$$

C. Application to the ROSE-L Case

In the case of ROSE-L, the accuracy is computed using the NESZ shown in Fig. 3, the AASR is shown in Fig. 4, and the parameters are listed in Table I.

Applying (8) and (9), the decorrelation due to the system noise can be computed. The decorrelation depends on the backscatter of the scene σ_0, with higher backscatter leading to higher SNR values and less decorrelation. Similarly, (11) is used to compute the decorrelation due to incoherent azimuth ambiguities. The coherence of each of the looks then follows from (7) and is shown in Fig. 5 as a function of the Doppler centroid frequency. It can be seen that the coherence depends on the position of the target within the burst. The lowest coherence can be found close to the burst edges for azimuth Doppler centroids $f_{\mathrm{DC}} = \pm 1988$ Hz (and slightly shifted if incoherent azimuth ambiguities are not considered), while the burst center preserves the highest coherence. Applying (6) and assuming a spectral distance $\Delta f = 1988$ Hz, the along-track deformation retrieval performance throughout the burst can be determined, as shown in Fig. 6. Due to the overlapping bursts, the retrieval performance is worst at the burst center and best at the edges of the single-look burst. Again, in case the incoherent azimuth ambiguities are not considered, the worst case position within the burst is slightly shifted. Exemplary values for the best case and worst case coherences, SNR, and AASR within a burst for a homogeneous scene are listed in Table III. The backscatter coefficient for these exemplary values is chosen as $\sigma_0 = -11$ dB, which is a reasonable value for rock and soil backscatter in the L band according to [25], and the temporal coherence is set to an exemplary value $\gamma_{\mathrm{TEMP}} = 0.7$, which is reasonable according to [26].

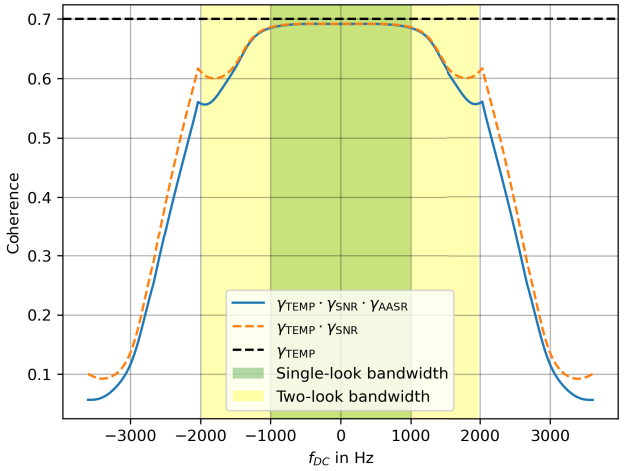

Fig. 5. Coherence of an interferogram within a scene depending on the Doppler centroid frequency. The plot shows the coherence for a scene with backscatter $\sigma_0 = -11$ dB and temporal coherence $\gamma_{\mathrm{TEMP}} = 0.7$. The blue curve represents the total coherence if temporal coherence, system noise, and incoherent azimuth ambiguities are taken into account, and the orange dashed curve represents the case without incoherent azimuth ambiguities and serves as a reference for the simulations in Section IV.

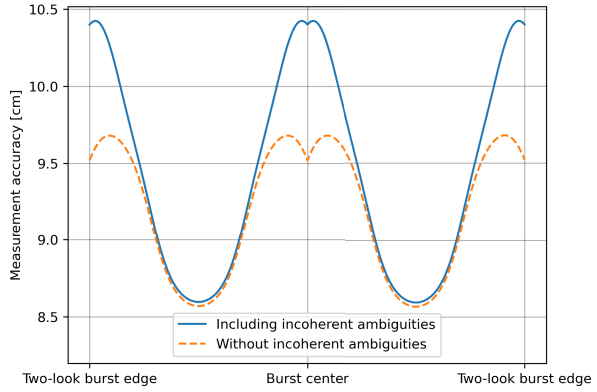

Fig. 6. Along-track deformation retrieval accuracy depending on the position within the two-look burst. An exemplary backscatter of $\sigma_0 = -11\,\text{dB}$ and temporal coherence $\gamma_{\text{TEMP}} = 0.7$, together with a spatial averaging using $N_{\text{looks}} = 50$ looks to reduce phase noise, are assumed in this example. The blue curve represents the accuracy if temporal coherence, system noise, and incoherent azimuth ambiguities are taken into account, and the orange dashed curve represents the case without incoherent azimuth ambiguities and serves as a reference for the simulations in Section IV.

TABLE III

REFERENCE VALUES FOR WORST CASE AND BEST CASE DISTRIBUTED TARGETS WITH $\sigma_0 = -11\,\text{dB}$ AND $\gamma_{\text{TEMP}} = 0.7$

	Look 1	**Look 2**
Worst Case	$f_{DC} = 0\,\text{Hz}$	$f_{DC} = 1988\,\text{Hz}$
SNR	19.2 dB	8.0 dB
γ_{SNR}	0.99	0.86
AASR	−41.1 dB	−10.6 dB
γ_{AASR}	1.00	0.92
γ_L	0.69	0.56
Best Case	$f_{DC} = -994\,\text{Hz}$	$f_{DC} = 994\,\text{Hz}$
SNR	17.3 dB	17.3 dB
γ_{SNR}	0.98	0.98
AASR	−28.1 dB	−28.1 dB
γ_{AASR}	1.00	1.00
γ_L	0.69	0.69

Fig. 7 shows the retrieval accuracy for $N_{\text{looks}} = 50$ looks as a function of the backscattering coefficient. An accuracy of less than 10 cm can be achieved for backscatter values $\sigma_0 \geq -19\,\text{dB}$ approximately for the best case and in the worst case for $\sigma_0 \geq -12\,\text{dB}$. This is a significant improvement of a factor of approximately 4–7 compared to the cross correlation case, which is limited by the azimuth resolution. The number of looks corresponds to a resolution of approximately 50 × 50 m in azimuth and ground range.

The previous analyses only consider the PRF of the first subswath of ROSE-L. In order to determine the validity of the results for the other subswaths as well, an analysis of the worst AASR within the processed bandwidth over different PRF values is shown in Fig. 8. The plots show that the worst AASR only varies by about 1 dB between the PRFs of the different subswaths. The SNR also slightly varies over different PRF values due to the different noise scaling of the MAPS reconstruction. Noise scaling will be highest in the first subswath due to the large distance to the uniform sampling PRF. The simulation results are thus also representative of lower bound for the other subswaths.

D. Role of Multilooking

The performance in the retrieval of the azimuth shift estimation, given by (6), can be only improved by means

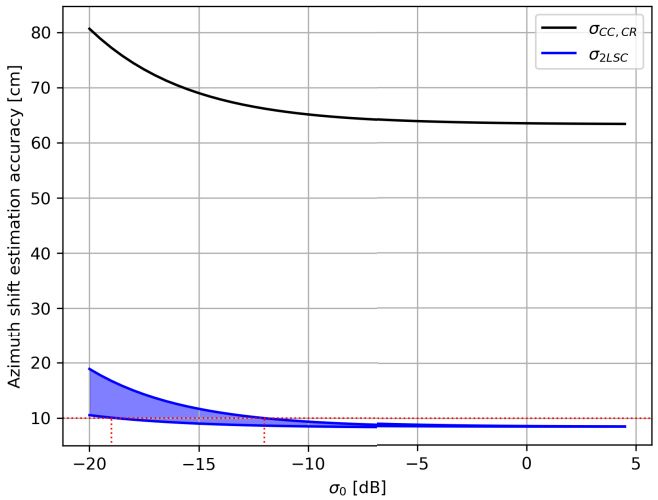

Fig. 7. Azimuth shift estimation accuracy over backscatter coefficient for single-look (black) and two-look retrieval (blue). For the two-look case, the accuracy depends on the position in the burst. Both accuracy estimates correspond to a multilooking with $N_{\text{looks}} = 50$ looks (or a resolution of 50 × 50 m). The red dotted lines mark the points where the best case and worse case achieve an accuracy of 10 cm.

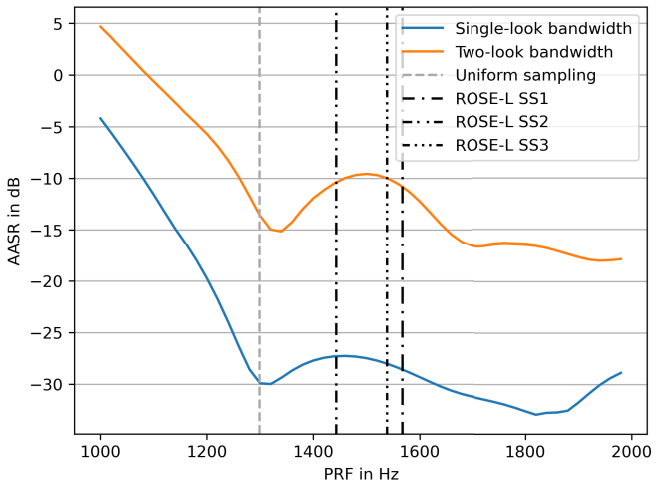

Fig. 8. Worst AASR in the azimuth bandwidth of a single-look and two-look burst. The black dashed-dotted vertical lines mark the PRFs currently under consideration for the different subswaths of ROSE-L in the dual-polarization mode, and the gray dashed vertical line marks the ideal PRF for which a uniform sampling is achieved with the system configuration of ROSE-L.

of a larger spatial averaging since all other parameters are intrinsically given by the system design or the scene characteristics. This imposes a clear tradeoff between accuracy and spatial resolution. The performance as a function of different multilooked resolutions is shown in Fig. 9, where an initial spatial resolution of 10 × 5 m in azimuth and ground range has been assumed. For each multilooked resolution, the best and worst case performances are shown.

As expected, the analysis shows that an increased number of looks results in a lower standard deviation of the error and a lower difference of best case and worst case accuracies within the burst.

E. Influence of Coherent Azimuth Ambiguities

Sections III-B and III-C have assumed uncorrelated azimuth ambiguities, hence behaving similar to noise, as can be clearly

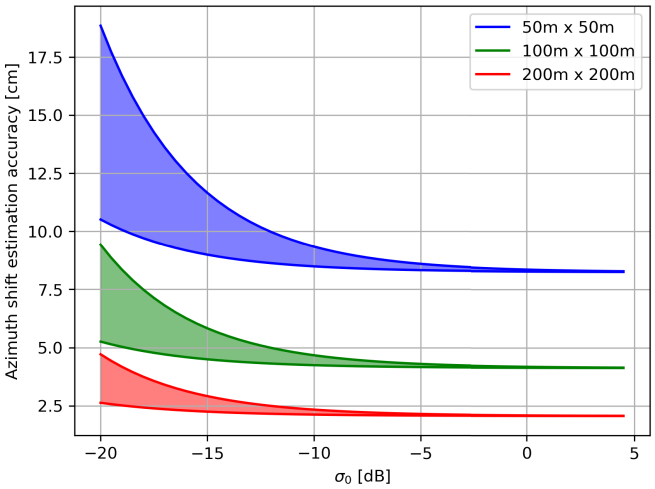

Fig. 9. Retrieval accuracy for different values of N_{looks}. The plot indicates the resulting resolutions in the azimuth and ground range, with the respective multilooking factors being—blue: $N_{\text{looks}} = 50$, green: $N_{\text{looks}} = 200$, and red: $N_{\text{looks}} = 800$.

concluded by comparing (9) and (11). This assumption might not be necessarily true, especially for SAR missions with a small orbital tube and, therefore, small interferometric baselines. In such cases, coherent azimuth ambiguities can result in interferometric biases in scenes with very heterogeneous backscattering and deformation signals [27].

To quantify the impact of these phase biases on the two-look product, we once again take distributed Gaussian scatterers as a model for the SAR signal. The looks are assumed to be independent, as the different looks' spectral portions of the clutter spectrum are uncorrelated. Thus, both looks can be simulated as independent interferograms.

In the following, a stochastic expression for the computation of the phase biases is derived. A more detailed analysis of the statistics of an SAR interferogram can be found in [23] and [28]. The joint probability density function (pdf) of magnitude $|v|$ and phase ψ of an interferogram is characterized by three parameters, which all describe the relation of the two interfering stochastic processes: the geometric mean power I, the magnitude of their complex coherence $|\gamma|$, and the expected value of their phase difference ϕ. The joint pdf is given by [28]

$$\text{pdf}(|v|, \psi) = \frac{2|v|}{\pi I^2\left(1-|\gamma|^2\right)} \exp\left\{\frac{2|\gamma||v|\cos(\psi-\phi)}{I\left(1-|\gamma|^2\right)}\right\} \times K_0\left(\frac{2|v|}{I\left(1-|\gamma|^2\right)}\right) \tag{12}$$

where $K_0(\cdot)$ is the modified Bessel function of order zero. In the following, we assume that the spectral diversity interferogram is generated after the multilooking of the interferograms, and therefore, we can continue the derivation with the expected values of the interferograms. The expected value of the interferogram v is then given as

$$\mathbb{E}\{v\} = I|\gamma|\exp\{j\phi\}. \tag{13}$$

The interferogram of the lth look, $l \in \{1, 2\}$, can be modeled as the sum of two independent stochastic processes as given in (12), representing main signal (subscript m) and ambiguity (subscript a) with resulting expectation [27]

$$\begin{aligned}\mathbb{E}\{v_l\} &= \mathbb{E}\{v_{m,l}\} + \mathbb{E}\{v_{a,l}\} \\ &= P_{m,l}|\gamma_{m,l}|\exp\{j\phi_{m,l}\} + P_{a,l}|\gamma_{a,l}|\exp\{j\phi_{a,l}\}\end{aligned} \tag{14}$$

where P is the power of the respective process. By recalling that both looks are independent stochastic processes v_1 and v_2 with the pdf given in (12), the expected value of the spectral diversity interferogram $v_{\text{sd}} = v_1 v_2^*$ (where * is the complex conjugation) can be written as

$$\begin{aligned}\mathbb{E}\{v_{\text{sd}}\} &= \mathbb{E}\{v_1 v_2^*\} = \mathbb{E}\{v_1\}\cdot\mathbb{E}\{v_2^*\} \\ &= \mathbb{E}\{v_{m,1}\}\mathbb{E}\{v_{m,2}^*\} + \mathbb{E}\{v_{m,1}\}\mathbb{E}\{v_{a,2}^*\} \\ &\quad + \mathbb{E}\{v_{a,1}\}\mathbb{E}\{v_{m,2}^*\} + \mathbb{E}\{v_{a,1}\}\mathbb{E}\{v_{a,2}^*\}\end{aligned} \tag{15}$$

where the first term of the sum corresponds to the main signal and the three remaining terms contribute to the phase bias. Note that due to the independence of the two looks and nonzero mean distributions (see (14), assuming the nontrivial case $I > 0$ for all contributions), in contrast to the case of a single interferogram (see [27]), also none of the additive terms is negligible.

Consequently, the phase bias $\phi_{\text{bias,sd}}$ follows as the difference of the complete spectral diversity phase ϕ_{sd} and the phase of the main signal $\phi_{m,\text{sd}}$, where the notation $|_{(-\pi,\pi]}$ refers to the phase projected to the interval $(-\pi, \pi]$, resulting in

$$\phi_{\text{bias,sd}} = \left(\phi_{\text{sd}} - \phi_{m,\text{sd}}\right)\big|_{(-\pi,\pi]} \tag{16}$$

$$\begin{aligned}&= \left(\arg\{\mathbb{E}\{v_{\text{sd}}\}\} - \arg\left\{\mathbb{E}\{v_{m,1}\}\mathbb{E}\{v_{m,2}^*\}\right\}\right)\big|_{(-\pi,\pi]} \\ &= \arg\left\{1 + \frac{\mathbb{E}\{v_{a,1}\}}{\mathbb{E}\{v_{m,1}\}} + \frac{\mathbb{E}\{v_{a,2}^*\}}{\mathbb{E}\{v_{m,2}^*\}} + \frac{\mathbb{E}\{v_{a,1}\}\mathbb{E}\{v_{a,2}\}^*}{\mathbb{E}\{v_{m,1}\}\mathbb{E}\{v_{m,2}\}^*}\right\} \\ &= \arg\left\{1 + \frac{P_{a,1}}{P_{m,1}}\frac{|\gamma_{a,1}|}{|\gamma_{m,1}|}\exp\{j(\phi_{a,1}-\phi_{m,1})\} \right. \\ &\quad + \frac{P_{a,2}}{P_{m,2}}\frac{|\gamma_{a,2}|}{|\gamma_{m,2}|}\exp\{-j(\phi_{a,2}-\phi_{m,2})\} \\ &\quad + \frac{P_{a,1}P_{a,2}}{P_{m,1}P_{m,2}}\frac{|\gamma_{a,1}||\gamma_{a,2}|}{|\gamma_{m,1}||\gamma_{m,2}|} \\ &\quad \left.\cdot\exp\{j\left[\left(\phi_{a,1}-\phi_{m,1}\right)-\left(\phi_{a,2}-\phi_{m,2}\right)\right]\}\right\}.\end{aligned} \tag{17}$$

When comparing this result to the phase bias of a single interferogram, as given in [27], it is easy to show that due to the independence of the looks, the phase bias of the spectral diversity interferogram corresponds to the difference of the biases of the two individual looks.

The power and coherence of the main signal and ambiguities depend on the parameters of the scene, e.g., the backscattering coefficients of main signal and ambiguity σ_m and σ_a and the temporal coherence, as well as on system parameters, more specifically the AASR. The power of main signals and ambiguities is computed as

$$P_m(f_{\text{DC}}) = \sigma_m \cdot G(f_{\text{DC}}) \tag{18}$$

$$P_a(f_{\text{DC}}) = \sigma_a \cdot G(f_{\text{DC}}) \cdot \text{AASR}(f_{\text{DC}}). \tag{19}$$

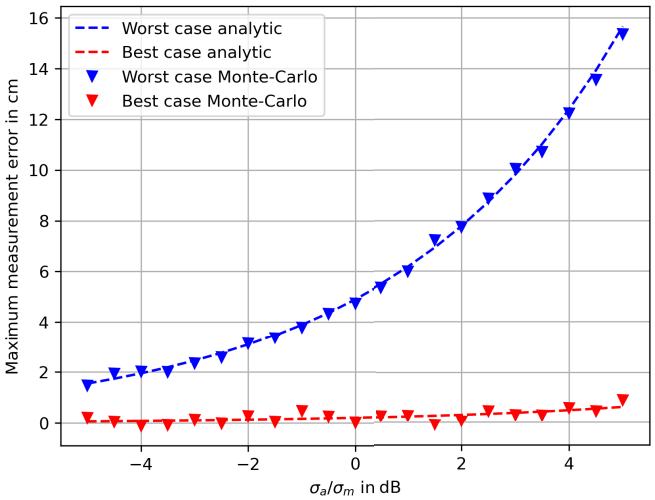

Fig. 10. Analytical and Monte Carlo results for the maximum measurement error due to the ambiguity phase bias in ROSE-L. σ_m and σ_a are the backscatter coefficients of the main signal and ambiguities, respectively.

For the coherences in this approach, it is enough to consider

$$\gamma_m = \gamma_a = \gamma_{\text{TEMP}} \tag{20}$$

as the decorrelation due to the SNR is effective on the combined ambiguous signal and does not change the magnitude of the ambiguity phase bias. In order to determine the maximum measurement errors in the spectral diversity interferogram, the maximum phase biases are computed according to (17) for the best case and worst case positions within the bursts and transformed to a measurement error with (2). Fig. 10 shows the resulting maximum error for the worst and best case positions in azimuth for the ROSE-L system. Note that the phase bias cannot be mitigated by increasing the number of looks. The bias furthermore depends on the ratios of ambiguity to signal power and coherence and is thus independent of the absolute sigma nought and coherence values of the scene.

IV. Experimental Validation

In order to verify the analytical results and to evaluate the performance in a more realistic scenario, an end-to-end simulation chain has been implemented, including a forward model and the retrieval approach as previously suggested. The simulation follows the general logic of end-to-end simulations as they have been implemented, e.g., in [29], and is explained in detail in Appendix D. Sections IV-A and IV-B show the results of the implemented simulations using different scenes to validate the analytical results and to show the behavior of the different error contributions within a realistic SAR image.

A. Homogeneous Scene

For the first evaluations, the scene is artificially generated as homogeneous clutter with a temporal decorrelation of $\gamma_{\text{TEMP}} = 0.7$, which shall allow a further validation of the analytical performance model derived in Section III.

1) Performance Validation: To validate the performance from Fig. 9, simulations with different σ_0 and different multilooking factors are evaluated. The inserted deformation is assumed to be zero to avoid biases due to ambiguities in the retrieved performance, as these are not part of the analytical performance model presented before. In this way, the measured signal consists only of errors caused by the inserted system noise and should match the theoretical analysis. Two different σ_0 values are chosen with $\sigma_0 = -11\,\text{dB}$ (see also Table III) and $\sigma_0 = -20\,\text{dB}$.

The accuracy of the retrieved along-track deformation measurement can be expressed by means of the standard deviation of the measurement error for different azimuth positions and is shown in Fig. 11 for $\sigma_0 = -11\,\text{dB}$ and in Fig. 12 for

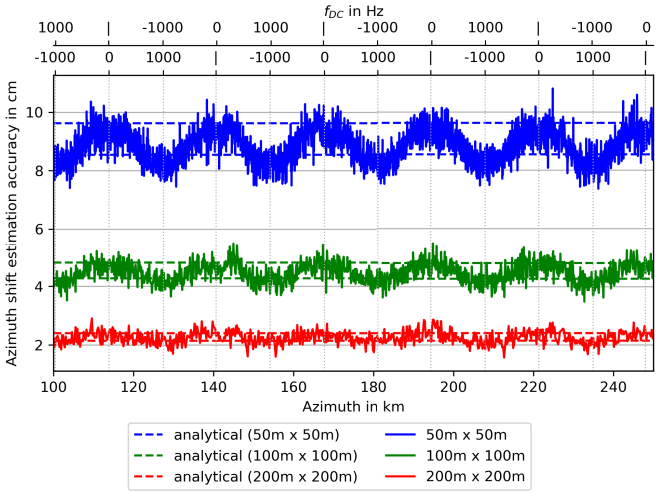

Fig. 11. Error standard deviation of the measured deformation along azimuth for simulated homogeneous backscatter with $\sigma_0 = -11\,\text{dB}$. Output resolutions of 50 × 50 m (blue), 100 × 100 m (green), and 200 × 200 m (red) in azimuth and ground range. The horizontal lines show the worst and best cases as predicted by the analytical formulation for the different numbers of looks (see Fig. 9). The axes on top of the plot give the Doppler centroid frequencies of the two overlapping looks for the respective points. The plot shows a cutout of the processed scene.

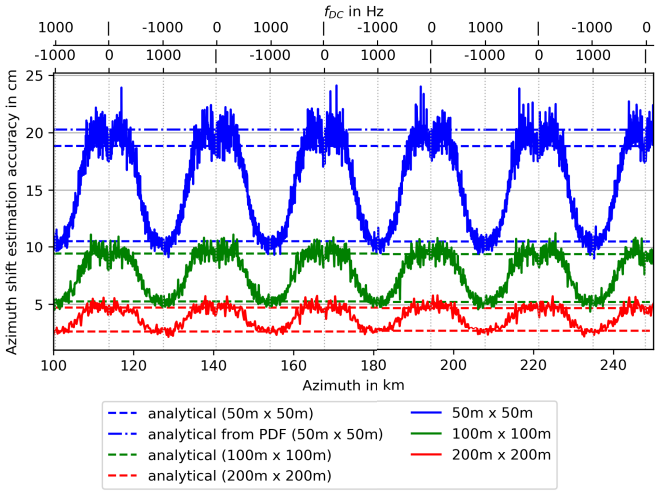

Fig. 12. Error standard deviation of the measured deformation along azimuth for simulated homogeneous backscatter with $\sigma_0 = -20\,\text{dB}$. Output resolutions of 50 × 50 m (blue), 100 × 100 m (green), and 200 × 200 m (red) in azimuth and ground range. The horizontal dashed lines show the worst and best cases as predicted by the analytical formulation for the different numbers of looks (see Fig. 9). For the worst case estimate of the 50 m multilooking, the approximated standard deviation [see (6)] becomes inaccurate due to the low coherence and the low number of looks. The blue dashed-dotted line shows the standard deviation derived from the pdf given in (12). The axes on top of the plot give the Doppler centroid frequencies of the two overlapping looks for the respective points. The plot shows a cutout of the processed scene.

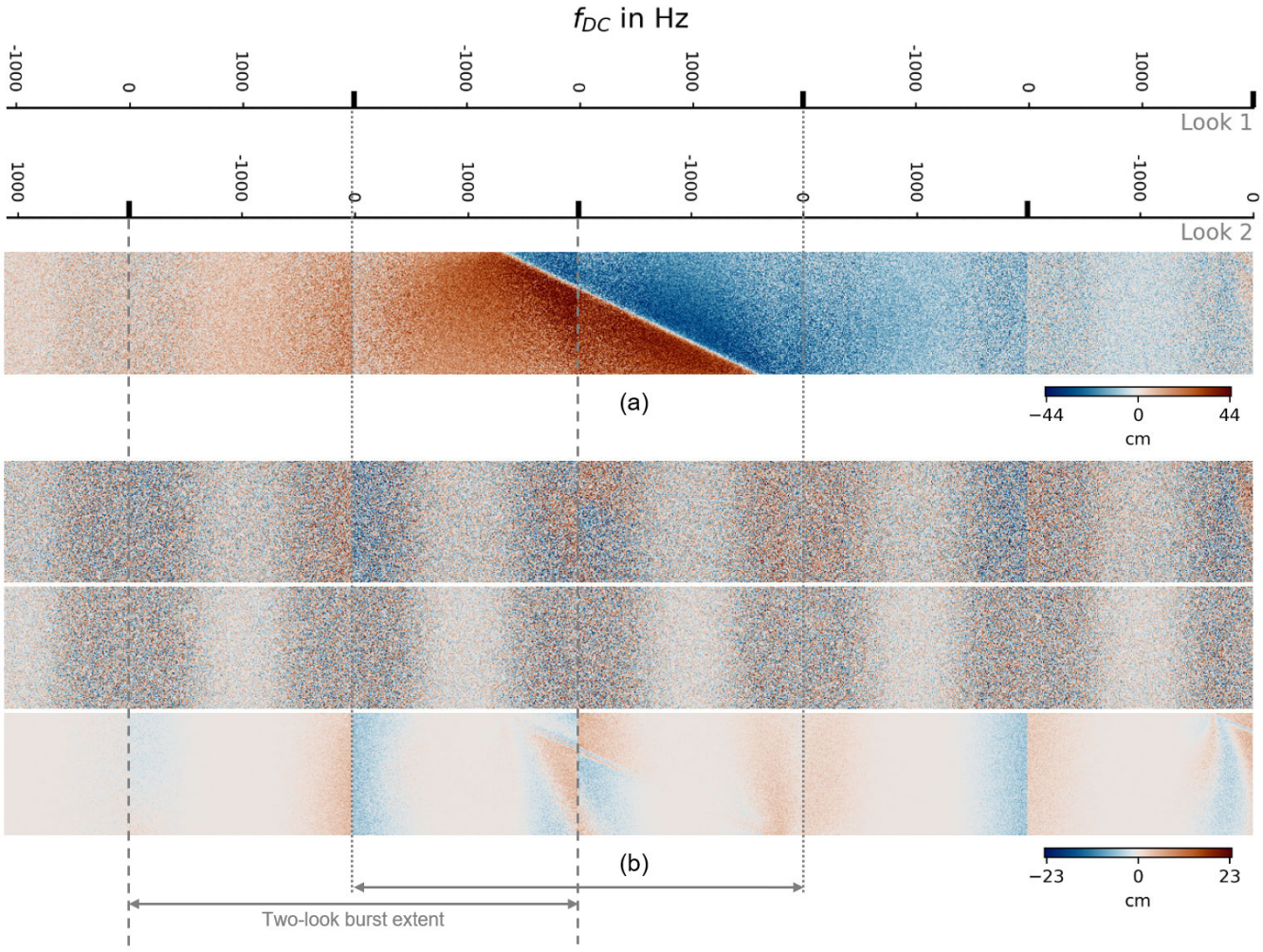

Fig. 13. Results of the simulations with a homogeneous scene, resolution of 100 × 100 m, spanning 150 km in azimuth (horizontal) and 15 km in ground range (vertical). (a) Retrieved along-track deformation. (b) From top to bottom: total measurement error, contribution of receiver noise, and contribution of coherent azimuth ambiguities. The figure shows a cutout of the complete processed scene, and the burst extents of two overlapping two-look bursts and their respective azimuth Doppler centroid frequencies at each point are marked.

$\sigma_0 = -20$ dB. As expected, the accuracy depends on the position of the target within the burst, while the best case and worst case accuracies mostly match the analytical results from Section III, shown by the horizontal dashed lines. The shape of the measured accuracies matches the expectation from the analytical computations, with the worst accuracy obtained close to the two-look burst edges. This is linked to the locally maximum NESZ value at these points (see Fig. 3).

2) Phase Bias: In order to evaluate the phase bias contribution as discussed in Section III, realizations of a scene with backscatter $\sigma_0 = -11$ dB are simulated with and without ambiguities, and these two results are compared in order to isolate the contribution of the phase bias. The deformation for this simulation is generated using the Okada model [30]. Fig. 13 shows the retrieved deformation, the total error, and the two main contributions to the error: receiver noise and azimuth ambiguities. The isolated error contribution due to the ambiguities has a maximum magnitude close to 5 cm, closely matching the analytical worst case prediction for a backscatter ratio $\sigma_a/\sigma_m = 0$ dB in Fig. 10, as expected for a scene with homogeneous backscatter. Note that, as mentioned in the analysis in Section III-E, the phase bias does not depend on the specific backscatter of the scene, but rather on the ambiguity to signal backscatter ratio. Thus, a simulation with a comparable homogeneous scene with $\sigma_0 = -20$ dB would result in the same phase bias.

B. Real Reflectivity Scene Simulations

In order to get a more realistic idea of the behavior of the different error contributions within a radar image, in the following, two different simulations are performed using real backscattering maps. The first one is set over the East Anatolian Fault and shows an artificial earthquake-like deformation. The second scene is set over the Petermann glacier in Greenland and uses a real deformation measurement as input.

Note that both scenarios are based on the reflectivity inputs generated from Sentinel-1 acquisitions at the C band, whereas ROSE-L works at the L band. This fact does not invalidate the results since the purpose of these simulations is to provide a realistic idea of how the different contributions affect the final

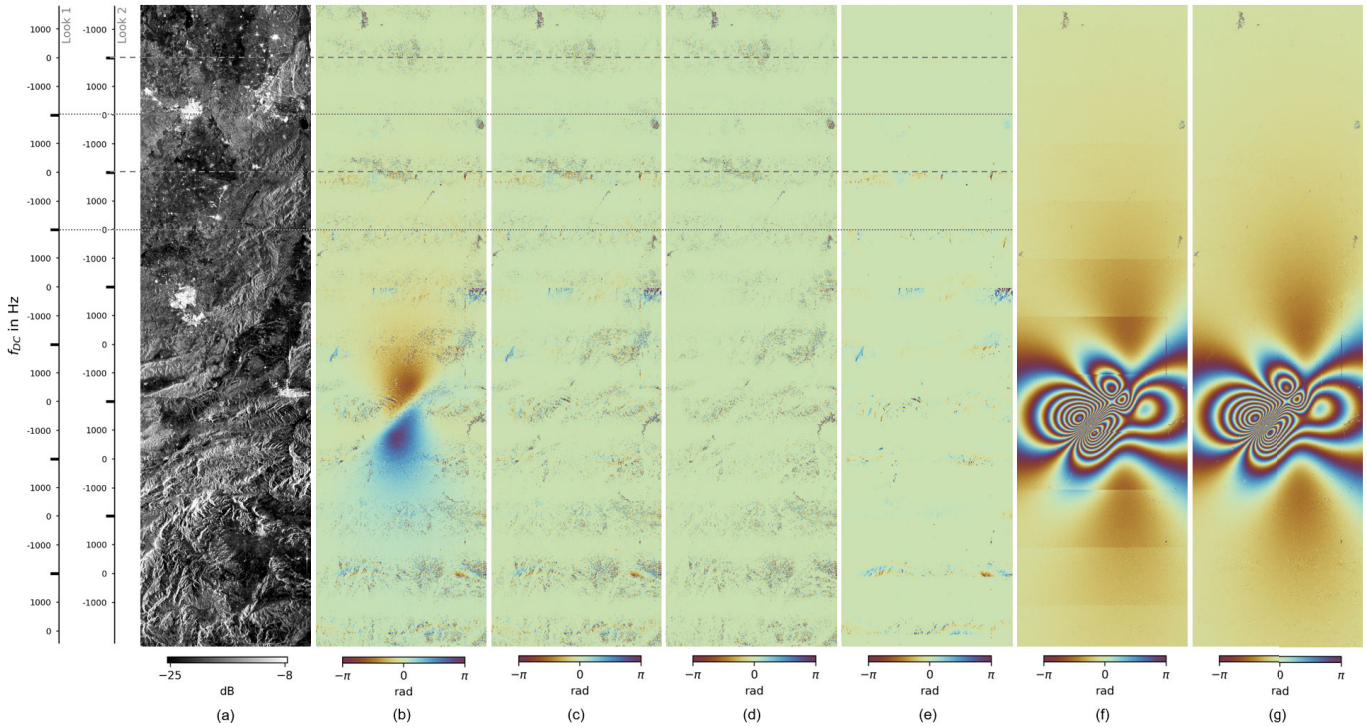

Fig. 14. Simulation results with the earthquake scenario, covering approximately 300 km in azimuth (vertical) and 80 km in ground range (horizontal), multilooked to a resolution of approximately 200 × 200 m. Dotted and dashed horizontal lines indicate the extent of two overlapping two-look bursts and the respective Doppler centroid frequencies, respectively. (a) Measured backscatter of the scene (sigma nought). (b) Retrieved spectral diversity interferometric phase. (c) Total phase error. (d) Phase error due to receiver noise. (e) Phase error due to azimuth ambiguities. (f) Single-look interferometric phase in line of sight. (g) Retrieved zero-Doppler interferometric phase after removing the along-track deformation. For the spectral diversity phases in (b)–(e), one phase cycle corresponds to a deformation of 3.59 m; for the single-look interferometric phases in (f) and (g), one phase cycle corresponds to a deformation of 12 cm. The horizontal dashed and dotted lines mark the extent of two overlapping bursts.

image quality for different spatial distributions of backscatter values. In this sense, the dynamic range of the reflectivity image is critical. Lower frequency bands tend to have a larger dynamic range in backscatter, but for this reason, two different scenarios with significantly different dynamic ranges have been selected.

On a second note, in the presented simulations, the (unwrapped) spectral diversity phase can easily be transformed to the corresponding deformation using a conversion factor of 3.59 m per phase cycle. However, highly decorrelated areas as well as areas with strong biases pose problems when applying state-of-the-art phase unwrapping algorithms, so the simplified phase unwrapping used for the simulations would produce better results than could be expected from actual algorithms. For this reason, the following results show the wrapped spectral diversity phase rather than the along-track deformation. Interested readers are referred to [31], [32], [33], [34], and [35] for a collection of applicable unwrapping algorithms.

1) Earthquake Scenario: The first scene is set over the East Anatolian Fault, where a descending Sentinel-1 acquisition from February 2023 is exploited to generate the amplitude for the simulation. The simulated scene covers one complete subswath of Sentinel-1 of about 80 km in ground range and 300 km in along-track. The deformation is again generated using the Okada model [30], assuming a fault with the approximate orientation and location of the East Anatolian Fault, and the temporal decorrelation is assumed constant with a value of $\gamma_{\mathrm{TEMP}} = 0.7$. The output resolution of the simulated results is multilooked to a resolution of 200 × 200 m in azimuth and ground range. Fig. 14 shows the retrieved spectral diversity phase of the inserted deformation in the along-track direction, the total error, the different components of the error, and the compensation of the along-track deformation in the line-of-sight interferogram as results of the simulation.

The decomposition of the error shows that the biases due to azimuth ambiguities occur toward the two-look burst edges and are mostly small compared to the main signal. The strongest component of the error is the error due to receiver noise. It is of random nature and shows a periodic spatial structure, which depends on the bursts and the reflectivity. The single-look interferogram in line of sight shows small phase jumps at the edges of the bursts, which can be compensated well with the measured deformation.

2) Glacier Scenario: The second scene is set over the Petermann glacier in Greenland, a fast-moving glacier, frequently observed by SAR satellites, for example, Sentinel-1 [3] or TerraSAR-X [8]. Again, the simulated scene covers one complete subswath of Sentinel-1 of about 80 km in the ground range and 300 km in the along-track. The reflectivity of a Sentinel-1 image acquired in December 2023 in the ascending mode is exploited for the simulation. The temporal decorrelation is set to $\gamma_{\mathrm{TEMP}} = 0.7$ and the deformation is taken from the Programme for Monitoring of the Greenland Ice Sheet (PROMICE) dataset for winter ice velocities over Greenland [36], [37]. The ice velocity field is transformed

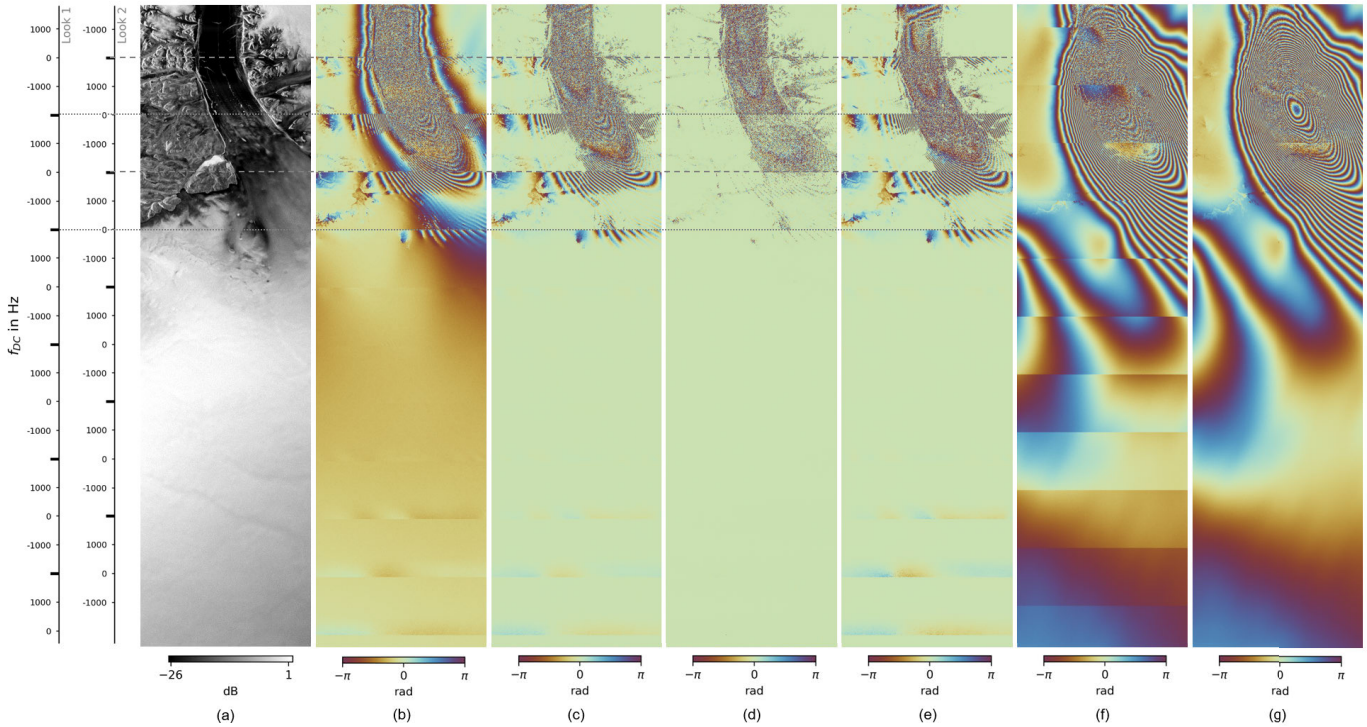

Fig. 15. Simulation results with the glacier scenario, covering approximately 300 km in azimuth (vertical) and 80 km in ground range (horizontal), multilooked to a resolution of approximately 200 m × 200 m. Dotted and dashed horizontal lines indicate the extent of two overlapping two-look bursts and the respective Doppler centroid frequencies, respectively. (a) Measured backscatter of the scene (sigma nought). (b) Retrieved spectral diversity interferometric phase. (c) Total phase error. (d) Phase error due to receiver noise. (e) Phase error due to azimuth ambiguities. (f) Single-look interferometric phase in line of sight. (g) Retrieved zero-Doppler interferometric phase after removing the along-track deformation. For the spectral diversity phases in (b)–(e), one phase cycle corresponds to a deformation of 3.59 m; for the single-look interferometric phases in (f) and (g), one phase cycle corresponds to a deformation of 12 cm. The horizontal dashed and dotted lines mark the extent of two overlapping bursts.

to absolute deformations corresponding to the planned revisit time of ROSE-L of 6 d, resulting in maximum (absolute) deformations of about 16-m along-track and 5-m across-track. The output resolution of the simulated results is multilooked to a resolution of 200 × 200 m in azimuth and ground range. Fig. 15 shows the results of the simulation. As in the previous example, the results show the impact of the different error sources on the retrieved signal, as well as the successful compensation of the along-track component of the interferometric phase in line of sight, which becomes obvious with the disappearance of the phase jumps between consecutive bursts.

The glacier tongue is highly decorrelated due to the large deformation as no coregistration was applied in the retrieval module. Note, however, that in areas with such large deformation patterns, coherent or incoherent cross correlation techniques are more suitable than interferometric techniques. In contrast to the earthquake scenario, the main contribution to the error in this scene is the biases due to the azimuth ambiguities. These become obvious in areas with low backscatter, such as around the tongue of the glacier, and, in particular, in areas corresponding spatially to the edges of the two-look bursts. As expected, the contribution of the receiver noise is particularly important in areas with low backscatter but negligible in areas with a strong signal. This particular scene represents an extreme case in terms of dynamic range, being larger than 25 dB. It is worth highlighting the high reflectivity of the middle part of the image, which is responsible for the observed biases around the glacier tongue in Fig 15(b). The biases show a periodic structure similar to the phase in line of sight, which can be explained with the model of the bias given in (17). This scenario is clearly a challenging one and has been selected to show the limitations of the technique in scenes with very heterogeneous reflectivities. For such a scenario, additional processing steps would be needed in order to either mitigate the biases introduced by the azimuth ambiguities [38], [39], [40] or by masking the areas where the signal-to-ambiguity ratio is smaller than a predefined threshold [41].

V. Conclusion and Future Work

This article has shown that the current design of the ROSE-L system allows for measurements of the along-track deformation using a two-look ScanSAR approach, which allows a retrieval accuracy beyond the performance that can be attained with the azimuth spatial resolution. The proposed approach shows a satisfactory performance for the current ROSE-L system design, hence keeping the quality performance for the nominal single-look image products. In order to be able to exploit the two-look approach, the ground processor would have to process a larger Doppler bandwidth, and consequently, the data storage requirements would have to be duplicated in the ground segment.

The final accuracy in the azimuth displacement retrieval depends on the target position within the overlapped bursts

and is limited by the two minima of the antenna pattern. Since the accuracy also depends on the multilooking and the radar backscattering coefficient of the scene, the difference in performance can be minimized by increasing the number of looks, however at the expense of spatial resolution. As an example, with a resolution of 100 × 100 m in azimuth and ground range, a mean accuracy of approximately 4.5 cm can be achieved for a region with a mean backscattering coefficient of −11 dB. In a subsequent step, the proposed processing approach allows the independent retrieval of the along-track and across-track deformations, and therefore, the combination of ascending and descending orbits would allow the retrieval of a 3-D deformation map.

Further simulations (not shown) have been performed by using an alternative antenna pattern, as suggested in [19]. In this case, the variability of the retrieval accuracy within the burst is reduced. This comes at the expense of a reduced peak antenna gain and thus results in a worse SNR and AASR within the single-look bandwidth. Additional investigations with alternative antenna patterns would be needed to evaluate whether the impact on the single-look images could be minimized.

The proposed approach might show significant phase biases due to coherent azimuth ambiguities in areas with spatially heterogeneous backscattering, as observed in the simulated results over the Petermann glacier. In order to improve these results, existing techniques to mitigate the azimuth ambiguities at interferogram level will be investigated, similar as suggested in [38], [39], and [40]. As another option, heavily biased values could be masked before the analysis, similar to the technique presented in [41] or by identifying them based on the reflectivity of the single-look signal and the expected space-variant ambiguity ratio considering the antenna pattern and MAPS.

Appendix A
Azimuth Doppler Bandwidths in ScanSAR

As in a conventional stripmap SAR system, the azimuth chirp rate, or Doppler rate of the azimuth chirp, for a ScanSAR acquisition is given by

$$k_{\mathrm{az}} = -\frac{2 \cdot v_{\mathrm{eff}}^2}{\lambda \cdot r_0} \tag{21}$$

where v_{eff} is the effective velocity, λ is the wavelength, and r_0 is the closest-approach distance. In ScanSAR, the temporal extent of each focused burst $T_{\mathrm{burst,foc}}$ is related to the focusing bandwidth B_{foc}, k_{az}, and the ScanSAR burst duration $T_{\mathrm{burst,raw}}$ or the bandwidth of a target B_{target} as follows:

$$\begin{aligned} T_{\mathrm{burst,foc}} &= B_{\mathrm{foc}}/|k_{\mathrm{az}}| - T_{\mathrm{burst,raw}} \\ &= \left(B_{\mathrm{foc}} - B_{\mathrm{target}}\right)/|k_{\mathrm{az}}|. \end{aligned} \tag{22}$$

As implied, the azimuth bandwidth of a target B_{target} (and thus also the azimuth resolution) directly depends on the burst duration $T_{\mathrm{burst,raw}}$ and both are connected by k_{az} with

$$B_{\mathrm{target}} = |k_{\mathrm{az}}| \cdot T_{\mathrm{burst,raw}}. \tag{23}$$

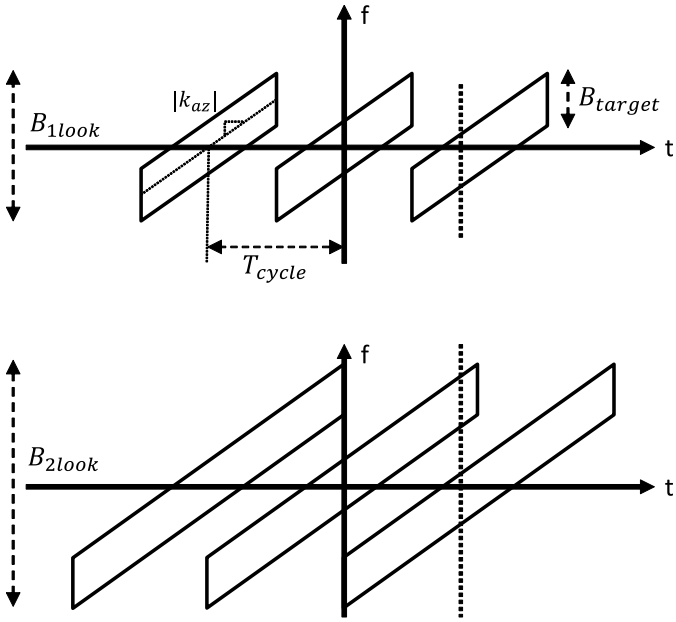

Fig. 16. Time–frequency diagrams of single-look and two-look ScanSAR. (Top) Single-look ScanSAR, the exemplary point marked with the dotted line in the right burst is covered once. (Bottom) Two-look ScanSAR, the same point is covered twice.

In order to have continuous coverage for all subswaths, $T_{\mathrm{burst,foc}}$ is set to the ScanSAR cycle time T_{cycle}, resulting in a minimum single-look bandwidth B_{1look} of

$$B_{\mathrm{1look}} = |k_{\mathrm{az}}| \cdot T_{\mathrm{cycle}} + B_{\mathrm{target}} \tag{24}$$

which corresponds to the scenario shown in the top of Fig. 16. According to (22), every target on ground can be covered by more than one burst by enhancing the processed bandwidth. The particular case shown in the lower time–frequency diagram in Fig. 16, where every target is covered by two different bursts, is referred to as two-look ScanSAR. With the approximate linear relation between time and frequency, the minimum required bandwidth for processing results in

$$B_{\mathrm{2look}} = 2 \cdot |k_{\mathrm{az}}| \cdot T_{\mathrm{cycle}} + B_{\mathrm{target}}. \tag{25}$$

Fig. 16 also shows that the two looks occupy different parts of the spectrum, leading to different Doppler centroid frequencies. The separation of these two Doppler centroids can be computed as

$$\Delta f = |k_{\mathrm{az}}| \cdot T_{\mathrm{cycle}}. \tag{26}$$

This spectral diversity is equivalent to different look angles and can be used to compute the relative shift in azimuth between two acquisitions.

Appendix B
Derivation of the System NESZ

This appendix derives the assumed NESZ curve shown in Fig. 3 from the system requirement for the NESZ given in Table II and the antenna pattern given in Fig. 1. A factor that additionally influences the system NESZ of ROSE-L is the

SNR scaling due to the beamforming in the MAPS reconstruction. The scaling factor $\Phi_{\text{bf}}(f)$ after the reconstruction of N channels is computed as [20]

$$\Phi_{\text{bf}}(f) = \frac{\sum_{j=0}^{N-1} |P_j(f)|^2}{N} \tag{27}$$

where $P_j(f)$ is the jth beamforming weight used in the reconstruction of the signal at azimuth Doppler frequency f.

The NESZ of the uncompressed data can then be derived from the inverse of the normalized two-way antenna gain $G(f)$, scaled by $\Phi_{\text{bf}}(f)$ and an arbitrary minimum NESZ NESZ_{min}, such that

$$\text{NESZ}(f) = \text{NESZ}_{\text{min}} \cdot \frac{\Phi_{\text{bf}}(f)}{G(f)}. \tag{28}$$

NESZ_{min} is chosen in a way such that the requirement given in Table II is tightly fulfilled. After compression with bandwidth B_D, the NESZ of a target with a given Doppler centroid frequency f_{DC} is then given as

$$\text{NESZ}_{B_D}(f_{\text{DC}}) = \mathbb{E}\big[\text{NESZ}(f) \cdot \text{rect}((f - f_{\text{DC}})/B_D)\big] \tag{29}$$

where the operator $\mathbb{E}[\cdot]$ indicates the computation of the mean value.

Appendix C
Analysis of Azimuth Ambiguities After Reconstruction and Focusing

This appendix derives the impact of the reconstruction and focuses on the power ratios of signal and azimuth ambiguities. When mentioning the AASR in Section III, the power ratio between ambiguities and signal after reconstruction and focusing AASR_{N,B_D} is referred to. Explanations and notation are largely based on [20], where the azimuth reconstruction algorithm used for the investigations shown in this article is presented.

The reconstruction algorithm uses N signals of bandwidth $B_{\text{ch}} = \text{PRF}$ to remove $(N-1)$ ambiguities from the main signal, creating a reconstructed signal of bandwidth given by (1). A signal of limited total bandwidth $B_{\text{sig}} = B_{\text{rec}}$ can thus be reconstructed without residual ambiguities, whereas any signal outside of this reconstructed bandwidth will remain as ambiguity. The ambiguous signals will be scaled by multiplicative weights $\mathbf{P}(f)$ depending on the channel and the reconstructed azimuth Doppler frequency interval $f_j = f_0 + j \cdot \text{PRF}$, $j = 0, \ldots, (N-1)$, which are given by [20]

$$\mathbf{P}(f_0) = \begin{bmatrix} P_{11}(f_0) & P_{12}(f_1) & \cdots & P_{1N}(f_{N-1}) \\ P_{21}(f_0) & P_{22}(f_1) & \cdots & P_{2N}(f_{N-1}) \\ \vdots & \vdots & \ddots & \vdots \\ P_{N1}(f_0) & P_{N2}(f_1) & \cdots & P_{NN}(f_{N-1}) \end{bmatrix}. \tag{30}$$

Due to the set of weights depending on the interval of the reconstructed azimuth frequency, the ambiguities have to be analyzed separately for each interval. Under the assumption of distributed scatterers, the ratio of azimuth ambiguities and main signal in the reconstructed signal (denoted as AASR_N) depends on the power of the signal p_s and the relevant ambiguous contributions p_a. Both are influenced by the antenna gain and the weighting of the reconstruction filters $P_{i(j+1)}$ for the relevant interval f_j. Fig. 17 shows the contributions of the main signal and the ambiguities for the reconstructed signal in the case of ROSE-L.

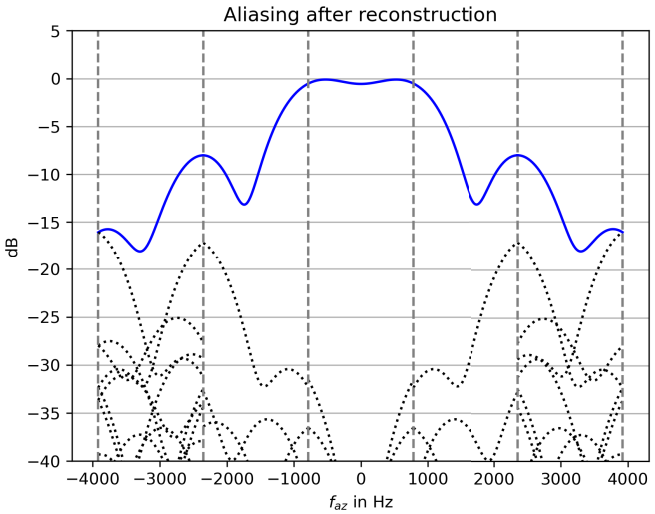

Fig. 17. Ambiguous contributions within the reconstructed signal. The main signal (blue) is reconstructed in five intervals, shown by the dashed lines. The magnitude of the ambiguities (dotted lines) depends on the reconstructed interval due to the beamforming weights of the reconstruction.

In the case of distributed scatterers, the computation of AASR_N differs slightly from the equation given in [20], where the respective ambiguous contributions e_k are added coherently. Here, due to the uncorrelated nature of the signals, the computation is given by

$$\text{AASR}_N(f) = \frac{p_a(f)}{p_s(f)} = \frac{\sum_{\forall k} |e_k(f)|^2}{p_s(f)}. \tag{31}$$

Focusing the signal with a Doppler bandwidth B_D corresponds to the computation of the mean value over the processed bandwidth for both signal and ambiguity power. The AASR_N of the focused signal with a given Doppler centroid frequency f_{DC} [denoted as $\text{AASR}_{B_D}(f_{\text{DC}})$] thus depends on the mean signal power over the focused bandwidth $p_{s,B_D}(f_{\text{DC}})$ and is given by

$$\text{AASR}_{B_D}(f_{\text{DC}}) = \frac{\mathbb{E}\big[\sum_{\forall k} |e_k(f)|^2 \cdot \text{rect}((f - f_{\text{DC}})/B_D)\big]}{p_{s,B_D}(f_{\text{DC}})}. \tag{32}$$

where the operator $\mathbb{E}[\cdot]$ indicates the computation of the mean value. The resulting $\text{AASR}_{B_D}(f_{\text{DC}})$ values for ROSE-L with $B_D = B_{\text{target}}$ are shown in Fig. 4.

Appendix D
Implementation of the Simulation

The simulation consists of the four main steps shown in Fig. 18 and can be split logically into a forward model (scene generation module and radar module), which generates the raw SAR data, and a simplified processing and analysis (retrieval module and evaluation module), which retrieve the signal of interest and compare it to the input.

The scene generation module creates a pair of synthetic SAR images of a scene that is subject to a known deformation. It takes as inputs as follows:

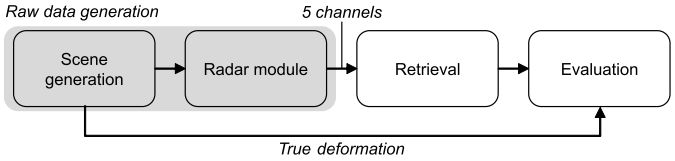

Fig. 18. Structure of the simulation. The scene generation module creates an interferometric pair of synthetic SAR images, and the radar module applies the effects of the multichannel synthetic aperture and the ScanSAR acquisition mode. The retrieval module consists of a simplified focusing and differential interferometric processing to retrieve the deformation values. Finally, the evaluation module compares the retrieved deformation to the true input deformation.

1) reflectivity image of a real acquisition or generated clutter;
2) temporal decorrelation, e.g., obtained from the interferometric coherence of a real image pair or based on a model;
3) 3-D deformation based on a model or real measurements.

It generates two complex SAR images of the same scene with the given coherence and interferometric phase. It performs the following steps sequentially.

1) Upsampling of the image to an azimuth sampling frequency of $\text{asf} = 15 \cdot \text{PRF}_{\text{ch}}$. This ensures access to the Doppler bandwidth after the reconstruction (factor 5 to PRF_{ch}) and the inclusion of the left and right azimuth ambiguities (additional factor of 3).
2) Generation of primary and secondary complex images by multiplying reflectivity data with complex Gaussian speckle according to the local temporal decorrelation,
3) Phase shift of the secondary acquisition according to the deformation in range.
4) The 2-D interpolation of the secondary acquisition according to deformation in azimuth and slant range.

For the sake of simplicity, a zero-baseline geometry is assumed, and therefore, no geometric distortions related to the scene topography are included in the simulation.

The radar module takes the two generated complex SAR images as input and computes the corresponding raw data considering the radar system characteristics. Hereby, the main steps are given as follows:

1) defocusing the images via azimuth decompression;
2) multiplication of the antenna pattern in the range–Doppler domain;
3) generation of the five azimuth raw data channels by multiplying with the corresponding residual bistatic impulse responses $H_i(f)$ (see the following for the expression of these filters);
4) decimation of each raw data channel in the azimuth dimension by a factor of 15 to retrieve a signal with a sampling equal to $\text{asf} = \text{PRF}_{\text{ch}}$ (and thus introducing coherent ambiguities);
5) addition of (independent) circular white Gaussian noise realizations to each channel with noise power p_n;
6) cutting of the stripmap raw data in order to generate the ScanSAR bursts.

The residual bistatic channel impulse responses in the Doppler domain $H_i(f_{\text{az}})$ for each channel $i \in \{1, \ldots, 5\}$ are given by the expression derived in [20]

$$H_i(f_{\text{az}}) = \exp\left(-j \cdot \frac{\pi \cdot \Delta x_i^2}{2\lambda \cdot R_0}\right) \cdot \exp\left(-j \frac{\pi \cdot \Delta x_i}{v_{\text{eff}}} \cdot f_{\text{az}}\right) \tag{33}$$

where Δx_i is the along-track distance of the ith receive aperture's phase center to the transmit aperture's phase center, λ is the carrier frequency's wavelength, and R_0 is the closest approach slant-range distance.

The injected noise power p_n is constant over the spectrum and can be computed with the minimum NESZ and adjusting for the incident angle θ_{inc} as

$$p_n = \frac{\text{NESZ}_{\text{min}}}{\sin \theta_{\text{inc}}}. \tag{34}$$

The retrieval module implements a simplified processing chain including two-look and modified single-look processing as shown in Fig. 2. The main steps are given as follows:

1) MAPS reconstruction;
2) focusing and azimuth antenna pattern compensation;
3) burst-wise computation of the interferograms;
4) multilooking;
5) two-look interferometric processing;
6) along-track deformation retrieval;
7) interpolation of the secondary image to remove along-track deformation;
8) interferometric processing and mosaicking of the primary and phase corrected secondary single-look acquisitions, obtaining the zero-Doppler interferometric phase.

Here, as a main result, the along-track deformation and the zero-Doppler deformation are obtained. Note that for the along-track deformation retrieval, a simplified phase unwrapping is applied, which uses information about the integer phase cycle obtained from the nominal deformation.

The evaluation module finally compares the retrieved products with the nominal ones in order to evaluate qualitatively and quantitatively the performance of the retrieval approach.

The different contributions to the total error can be computed by modifying the ingested errors in the radar module for different simulations and then comparing their outputs. To determine the contribution of the thermal noise only, the error difference of simulations with and without thermal noise is computed, whereas for determining the influence of azimuth ambiguities, the errors of an ambiguity-free signal and one with ambiguities are compared. The ambiguity-free signal is hereby simulated by limiting the oversampled signal to a bandwidth of $B = 5 \cdot \text{PRF}_{\text{ch}}$.

ACKNOWLEDGMENT

The authors would like to thank Andrea Pulella for preprocessing the ice velocity data. They would also like to acknowledge and thank the anonymous reviewers for their helpful comments and suggestions, which greatly improved the quality of the article. Further acknowledgment goes to David Tomsu for the implementation of the first version of the simulation in an early stage of the study. Ice velocity maps were produced as part of PROMICE using Copernicus Sentinel-1 SAR images distributed by ESA and were

provided by the Geological Survey of Denmark and Greenland (GEUS) at http://www.promice.dk. This article uses the Scientific color maps vik and romaO [42] to prevent visual distortion of the data and exclusion of readers with color-vision deficiencies [43].

REFERENCES

[1] J. Biggs and T. J. Wright, "How satellite InSAR has grown from opportunistic science to routine monitoring over the last decade," *Nature Commun.*, vol. 11, no. 1, pp. 1–4, Aug. 2020, doi: 10.1038/s41467-020-17587-6.

[2] M. C. Araya and J. Biggs, "Towards a geodetic earthquake catalogue for Central America: Detecting coseismic deformation in Costa Rica using Sentinel-1 InSAR," *Geophys. J. Int.*, vol. 237, no. 1, pp. 145–158, Jan. 2024.

[3] R. Millan et al., "Ongoing grounding line retreat and fracturing initiated at the Petermann Glacier ice shelf, Greenland, after 2016," *Cryosphere*, vol. 16, no. 7, pp. 3021–3031, Aug. 2022. [Online]. Available: https://tc.copernicus.org/articles/16/3021/2022/

[4] R. Scheiber and A. Moreira, "Coregistration of interferometric SAR images using spectral diversity," *IEEE Trans. Geosci. Remote Sens.*, vol. 38, no. 5, pp. 2179–2191, Sep. 2000.

[5] N. B. D. Bechor and H. A. Zebker, "Measuring two-dimensional movements using a single InSAR pair," *Geophys. Res. Lett.*, vol. 33, no. 16, pp. 1–5, Aug. 2006, doi: 10.1029/2006gl026883.

[6] K. Tomiyasu, "Conceptual performance of a satellite borne, wide swath synthetic aperture radar," *IEEE Trans. Geosci. Remote Sens.*, vol. GE-19, no. 2, pp. 108–116, Apr. 1981.

[7] P. Prats-Iraola et al., "Repeat-pass interferometric experiments with the Tandem-X constellation for accurate along-track motion estimation," in *Proc. IEEE Int. Geosci. Remote Sens. Symp. (IGARSS)*, Jul. 2015, pp. 4077–4080.

[8] N. Yague-Martinez, P. Prats-Iraola, T. Kraus, S. Wollstadt, and R. Scheiber, "Experimental validation with TerraSAR-X/TanDEM-X of advanced interferometric modes for accurate retrieval of azimuthal displacements," in *Proc. IEEE Int. Geosci. Remote Sens. Symp. (IGARSS)*, Jul. 2016, pp. 1444–1447.

[9] N. Yague-Martinez, P. Prats-Iraola, S. Wollstadt, and A. Moreira, "The 2-look TOPS mode: Design and demonstration with TerraSAR-X," *IEEE Trans. Geosci. Remote Sens.*, vol. 57, no. 10, pp. 7682–7703, Oct. 2019.

[10] R. Grandin, E. Klein, M. Métois, and C. Vigny, "Three-dimensional displacement field of the 2015 M_w8.3 Illapel earthquake (Chile) from across- and along-track Sentinel-1 TOPS interferometry," *Geophys. Res. Lett.*, vol. 43, no. 6, pp. 2552–2561, Mar. 2016, doi: 10.1002/2016gl067954.

[11] Z.-F. Ma et al., "Challenges and prospects to time series burst overlap interferometry (BOI): Some insights from a new BOI algorithm test over the Chaman fault," *IEEE Trans. Geosci. Remote Sens.*, vol. 60, 2022, Art. no. 5118219.

[12] N. Yague-Martinez and P. Prats-Iraola, "Accurate azimuth ground deformation estimation from Sentinel-1 time series," *IEEE Geosci. Remote Sens. Lett.*, vol. 19, pp. 1–5, 2022.

[13] A. Pepe, P. Mastro, F. Falabella, and F. Calò, "Synthetic aperture radar burst overlapped interferometry (BOI) and multiple aperture interferometry (MAI) for the analysis of large ground instabilities: Experiments in mining and volcanic sites," in *Proc. IEEE Int. Geosci. Remote Sens. Symp.*, Jul. 2023, pp. 1956–1959.

[14] C. Liang and E. J. Fielding, "Measuring azimuth deformation with L-band ALOS-2 ScanSAR interferometry," *IEEE Trans. Geosci. Remote Sens.*, vol. 55, no. 5, pp. 2725–2738, May 2017.

[15] M. Davidson et al., "Rose-L—The Copernicus L-band synthetic aperture radar imaging mission," in *Proc. IEEE Int. Geosci. Remote Sens. Symp.*, Jul. 2023, pp. 4568–4571.

[16] D. Petrolati et al., "An overview of the Copernicus Rose-L SAR instrument," in *Proc. IEEE Int. Geosci. Remote Sens. Symp.*, Jul. 2023, pp. 4310–4313.

[17] G. Krieger, N. Gebert, and A. Moreira, "Unambiguous SAR signal reconstruction from nonuniform displaced phase center sampling," *IEEE Geosci. Remote Sens. Lett.*, vol. 1, no. 4, pp. 260–264, Oct. 2004.

[18] M. Suess, B. Grafmueller, and R. Zahn, "A novel high resolution, wide swath SAR system," in *Proc. Scanning Present Resolving Future, IEEE Int. Geosci. Remote Sens. Symp. (IGARSS)*, Jul. 2001, pp. 1013–1015.

[19] S. Perna, F. Longo, S. Zoffoli, M. Davidson, L. Iannini, and R. Lanari, "A conceptual performance study on a two-look ScanSAR mode configuration for the forthcoming ROSE-L mission," *IEEE Trans. Geosci. Remote Sens.*, vol. 62, 2023, Art. no. 5201618.

[20] N. Gebert, G. Krieger, and A. Moreira, "Digital beamforming on receive: Techniques and optimization strategies for high-resolution wide-swath SAR imaging," *IEEE Trans. Aerosp. Electron. Syst.*, vol. 45, no. 2, pp. 564–592, Apr. 2009.

[21] R. Bamler and M. Eineder, "Accuracy of differential shift estimation by correlation and split-bandwidth interferometry for wideband and delta-k SAR systems," *IEEE Geosci. Remote Sens. Lett.*, vol. 2, no. 2, pp. 151–155, Apr. 2005.

[22] T. J. Wright, B. E. Parsons, and Z. Lu, "Toward mapping surface deformation in three dimensions using InSAR," *Geophys. Res. Lett.*, vol. 31, no. 1, pp. 1–5, Jan. 2004.

[23] D. Just and R. Bamler, "Phase statistics of interferograms with applications to synthetic aperture radar," *Appl. Opt.*, vol. 33, no. 20, p. 4361, Jul. 1994.

[24] G. Krieger et al., "TanDEM-X: A satellite formation for high-resolution SAR interferometry," *IEEE Trans. Geosci. Remote Sens.*, vol. 45, no. 11, pp. 3317–3341, Nov. 2007.

[25] F. T. Ulaby and M. C. Dobson, *Handbook of Radar Scattering Statistics for Terrain*. Norwood, MA, USA: Artech House, 1989.

[26] A. Parizzi, X. Y. Cong, and M. Eineder, "First results from multifrequency interferometry. A comparison of different decorrelation time constants at L, C, and X band," in *Proc. ESA Sci. Publications*, Dec. 2009, p. 5. [Online]. Available: https://elib.dlr.de/62497/

[27] M. Villano and G. Krieger, "Impact of azimuth ambiguities on interferometric performance," *IEEE Geosci. Remote Sens. Lett.*, vol. 9, no. 5, pp. 896–900, Sep. 2012.

[28] R. Bamler and P. Hartl, "Synthetic aperture radar interferometry," *Inverse Problems*, vol. 14, no. 4, pp. R1–R54, Aug. 1998.

[29] M. Rodriguez-Cassola et al., "End-to-end level-0 data simulation tool for future spaceborne SAR missions," in *Proc. 12th Eur. Conf. Synth. Aperture Radar*, Jun. 2018, pp. 1–6.

[30] Y. Okada, "Surface deformation due to shear and tensile faults in a half-space," *Bull. Seismolog. Soc. Amer.*, vol. 75, no. 4, pp. 1135–1154, Aug. 1985.

[31] R. M. Goldstein, H. A. Zebker, and C. L. Werner, "Satellite radar interferometry: Two-dimensional phase unwrapping," *Radio Sci.*, vol. 23, no. 4, pp. 713–720, Jul. 1988.

[32] J. R. Buckland, J. M. Huntley, and S. R. E. Turner, "Unwrapping noisy phase maps by use of a minimum-cost-matching algorithm," *Appl. Opt.*, vol. 34, no. 23, p. 5100, Aug. 1995.

[33] D. C. Ghiglia and M. D. Pritt, *Two-Dimensional Phase Unwrapping*. Hoboken, NJ, USA: Wiley, 1998.

[34] H. Yu, Y. Lan, Z. Yuan, J. Xu, and H. Lee, "Phase unwrapping in InSAR: A review," *IEEE Geosci. Remote Sens. Mag.*, vol. 7, no. 1, pp. 40–58, Mar. 2019.

[35] C. W. Chen and H. A. Zebker, "Two-dimensional phase unwrapping with use of statistical models for cost functions in nonlinear optimization," *J. Opt. Soc. Amer. A, Opt. Image Sci.*, vol. 18, no. 2, p. 338, Feb. 2001.

[36] A. Solgaard and A. Kusk, 2021, "Winter ice velocity mosaics for the Greenland ice sheet from Sentinel-1 Edition 1," doi: 10.22008/FK2/8BM1IZ.

[37] A. Solgaard et al., "Greenland ice velocity maps from the PROMICE project," *Earth Syst. Sci. Data*, vol. 13, no. 7, pp. 3491–3512, Jul. 2021.

[38] A. M. Guarnieri, "Adaptive removal of azimuth ambiguities in SAR images," *IEEE Trans. Geosci. Remote Sens.*, vol. 43, no. 3, pp. 625–633, Mar. 2005.

[39] P. López-Dekker, Y. Li, L. Iannini, P. Prats-Iraola, and M. Rodríguez-Cassola, "On azimuth ambiguities suppression for short-baseline along-track interferometry: The stereoid case," in *Proc. IEEE Int. Geosci. Remote Sens. Symp.*, Jul. 2019, pp. 110–113.

[40] D. Richter, M. Rodriguez-Cassola, M. Zonno, and P. Prats-Iraola, "Coherent azimuth ambiguity suppression based on linear optimum filtering of short along-track baseline SAR interferograms," in *Proc. 14th Eur. Conf. Synth. Aperture Radar*, Jul. 2022, pp. 1–5.

[41] N. Petrushevsky and A. Monti Guarnieri, "Calibration of SIMO formations with azimuth ambiguities," *IEEE Trans. Geosci. Remote Sens.*, vol. 62, 2024, Art. no. 5209010.

[42] F. Crameri, Oct. 2023, "Scientific colour maps," doi: 10.5281/zenodo.8409685.

[43] F. Crameri, G. E. Shephard, and P. J. Heron, "The misuse of colour in science communication," *Nature Commun.*, vol. 11, no. 1, pp. 1–10, Oct. 2020.

Simon Trumpf received the B.Sc. and M.Sc. degrees in electrical engineering and information technology from Karlsruhe Institute of Technology (KIT), Karlsruhe, Germany, in 2018 and 2021, respectively. His master thesis focused on the analysis of the deformation retrieval accuracy of ESA's Earth Explorer 10 Multistatic Synthetic Aperture Radar (SAR) Harmony mission using end-to-end simulations. He is currently pursuing the Ph.D. degree with the German Aerospace Center (DLR), Weßling, Germany, and KIT, with a focus on the retrieval of 3-D deformation measurements with future SAR modes and mission concepts.

In 2020, he joined the Microwaves and Radar Institute, DLR. His research interests include differential SAR interferometry, end-to-end SAR simulation, and SAR systems performance evaluation.

Pau Prats-Iraola (Fellow, IEEE) was born in Madrid, Spain, in 1977. He received the Ingeniero and Ph.D. degrees in telecommunications engineering from the Universitat Politècnica de Catalunya (UPC), Barcelona, Spain, in 2001 and 2006, respectively.

In 2001, he was a Research Assistant at the Institute of Geomatics, Barcelona. In 2002, he was at the Department of Signal Theory and Communications, UPC, where he worked in the field of airborne repeat-pass interferometry and airborne differential synthetic aperture radar (SAR) interferometry. From December 2002 to August 2006, he was an Assistant Professor at the Department of Telecommunications and Systems Engineering, Universitat Autònoma de Barcelona, Barcelona. In 2006, he joined the Microwaves and Radar Institute, German Aerospace Center (DLR), Weßling, Germany, where he has been the Head of the Multimodal Algorithms Group since 2009. He is the responsible and main developer of the TanDEM-X Interferometric (TAXI) processor, an end-to-end processing chain for data acquired by the TerraSAR-X and TanDEM-X satellites, which has been used to demonstrate novel SAR acquisition modes and techniques. He is currently involved in the design and implementation of the ground processor prototypes and end-to-end simulators of ESA's BIOMASS, ROSE-L, and Harmony missions. His research interests include high-resolution airborne/spaceborne monostatic/bistatic SAR processing, SAR interferometry, advanced interferometric acquisition modes, persistent scatterer interferometry (PSI), SAR tomography, and end-to-end SAR simulation. He has co-authored more than 70 peer-reviewed journal articles in these fields.

Alberto Moreira (Fellow, IEEE) received the bachelor's and master's degrees in electrical engineering from the Aeronautical Technological Institute (ITA), São José dos Campos, Brazil, in 1984 and 1986, respectively, and the Ph.D. degree (Hons.) from the Technical University of Munich, Munich, Germany, in 1993.

From 1996 to 2001, he was the Head of the Synthetic Aperture Radar (SAR) Technology Department, German Aerospace Center (DLR), Weßling, Germany. Under his leadership, the DLR airborne SAR system has been upgraded to operate in innovative imaging modes such as polarimetric SAR interferometry, tomography, and holography. Since 2001, he has been the Director of the Microwaves and Radar Institute, DLR, and a Professor with Karlsruhe Institute of Technology (KIT), Karlsruhe, Germany, in the field of microwave remote sensing. His DLR's Institute contributes to several scientific programs and projects for spaceborne SAR missions such as TerraSAR-X, TanDEM-X, SAR-Lupe, and SARah, as well as Kompsat-6, PAZ, Sentinel-1, BIOMASS, ROSE-L, Harmony, Sentinel-1NG, Envision, and VERITAS. The mission TanDEM-X, led by his Institute, has generated a global, high-resolution digital elevation model of the Earth with unprecedented accuracy. He is the initiator and the principal investigator (PI) for this mission. He has served as a member for the ESA Mission Advisory Groups of ENVISAT/ASAR, Sentinel-1, Hydroterra, and EnVision and is currently serving as a member for Hydroterra+. He is the author or the co-author of more than 500 publications in international conferences and journals, and eight book chapters. He holds more than 45 international patent grants in the radar and antenna field. His professional interests and research areas encompass spaceborne radar end-to-end system design, microwave techniques and system concepts, signal processing, and remote sensing applications.

Prof. Moreira was a recipient of several international awards, including the IEEE Aerospace and Electronic Systems Society (AESS) Fred Nathanson Award in 1999, the IEEE Kiyo Tomiyasu Technical Field Award in 2007, the IEEE W. R. G. Baker Award from the IEEE Board of Directors in 2012, the IEEE GRSS Distinguished Achievement Award in 2014, and the IEEE Dennis J. Picard Medal for Radar Technologies and Applications in 2023. He and his colleagues received the GRSS Transactions Prize Paper Awards in 1997, 2001, and 2007, and the GRSS Letters Prize Paper Award in 2015 and 2017. He has served as the President for the IEEE Geoscience and Remote Sensing Society (GRSS) in 2010, the General Co-Chair for IEEE International Geoscience and Remote Sensing Symposium (IGARSS) in 2012, and the General Chair for EUSAR in 2006. He was the Founder and the Chair of the GRSS German Chapter from 2003 to 2008. He served as an Associate Editor for IEEE GEOSCIENCE AND REMOTE SENSING LETTERS from 2003 to 2007. He has been serving as an Associate Editor for IEEE TRANSACTIONS ON GEOSCIENCE AND REMOTE SENSING since 2005 and the Chair for the Major Awards of GRSS since 2017.